

Revisiting Rat Spermatogenesis with MALDI Imaging at 20- μ m Resolution*[§]

Mélanie Lagarrigue‡§¶, Michael Becker§||, Régis Lavigne‡, Sören-Oliver Deininger||, Axel Walch**‡‡, Florence Aubry‡, Detlev Suckau||§§, and Charles Pineau‡¶¶¶

Matrix-assisted laser desorption/ionization (MALDI) molecular imaging technology attracts increasing attention in the field of biomarker discovery. The unambiguous correlation between histopathology and MALDI images is a key feature for success. MALDI imaging mass spectrometry (MS) at high definition thus calls for technological developments that were established by a number of small steps. These included tissue and matrix preparation steps, dedicated lasers for MALDI imaging, an increase of the robustness against cell debris and matrix sublimation, software for precision matching of molecular and microscopic images, and the analysis of MALDI imaging data using multivariate statistical methods. The goal of these developments is to approach single cell resolution with imaging MS. Currently, a performance level of 20- μ m image resolution was achieved with an unmodified and commercially available instrument for proteins detected in the 2–16-kDa range. The rat testis was used as a relevant model for validating and optimizing our technological developments. Indeed, testicular anatomy is among the most complex found in mammalian bodies. In the present study, we were able to visualize, at 20- μ m image resolution level, different stages of germ cell development in testicular seminiferous tubules; to provide a molecular correlate for its well established stage-specific classification; and to identify proteins of interest using a top-down approach and superimpose molecular and immunohistochemistry images. *Molecular & Cellular Proteomics* 10:10.1074/mcp.M110.005991, 1–11, 2011.

MALDI imaging mass spectrometry (IMS)¹ is increasingly recognized as a powerful approach for the discovery of tissue

biomarkers candidates and tissue leakage products in clinical proteomics (1–6). The technology holds an enormous potential for differentiation of disease states, classification of tumors, and early diagnosis or prognosis but also for elucidating pathogenesis pathways and as a follow-up for pharmacological treatments (1, 7–9).

IMS offers some unique advantages that can support or complement most conventional techniques. It allows multiplex spatial localization of biomolecules on tissue sections without the need for time-consuming processing steps, specific probes, or labeling of analytes that can alter their native localization or function (10). Interestingly, in the field of biomarker detection, it is now recognized that in many cases a single protein cannot serve as a reliable disease-specific marker, whereas a panel of biomarkers candidates can potentially provide a clear diagnosis (8, 11). Although well established and extremely powerful, conventional differential proteomics approaches based on the analysis of tissue homogenates represent an oversimplification of tissue morphology in a “black versus white” manner (even if combined with tissue microdissection). In particular, cancer tissue consists of several different cell types at various developmental stages (12). An efficient, sensitive, and selective analysis of tumor tissue, therefore, ultimately requires the ability to perform molecular histological analyses on the level of individual cells.

Many technical challenges remain to be faced in IMS among which the improvement of lateral resolution, which is currently in the range of 100–200 μ m corresponding, at the best, to a few cells. Lateral resolution is mainly limited by the matrix application step and the laser beam diameter and shape, whereas reduction of the irradiated sample area naturally reduces the ion yield. Consequently, a compromise between high lateral resolution and spectral quality has generally to be found (13). However, the adequate evaluation of histological images after conventional hematoxylin and eosin (H&E) or immunohistological stainings routinely requires higher resolution down to the level of individual cellular nuclei. To beneficially integrate MALDI images into the histo(patho)-logical evaluation, there are two key requirements. 1) MALDI images should have utmost resolution to correlate them with the tissue morphology at least on the level of single cells (*i.e.* 10 μ m). 2) Overlapping of the transmission microscopic and MALDI images is mandatory to correlate molecular marker

From the ‡INSERM U625, Proteomics Core Facility Biogenouest, Campus de Beaulieu, Université de Rennes I, F-35042 Rennes, France, ||Bruker Daltonik GmbH, Fahrenheitstrasse 4, D-28359 Bremen, Germany, and **Helmholtz Zentrum München-German Research Center for Environmental Health, Institute of Pathology, Ingolstädter Landstrasse 1, 85764 Neuherberg, Germany

Received November 2, 2010, and in revised form, November 29, 2010

Published, MCP Papers in Press, December 12, 2010, DOI 10.1074/mcp.M110.005991

¹ The abbreviations used are: IMS, imaging mass spectrometry; ITO, indium tin oxide; Nd:YAG, neodymium-doped yttrium aluminium garnet; RP, reverse phase; LTQ, linear ion trap; AcSDKP, *N*-acetylseryl-aspartyl-lysyl-proline; ACSL, long-chain-fatty-acid-CoA ligase.

distributions with tissue morphology at typical microscopic image resolution (i.e. ~ 100 nm). One of the driving forces behind improvement of lateral resolution is that the detection of biomarker candidates can thus be confined to very fine structures of the tissue and even single cells. Improvements in resolution, which is indeed a methodological challenge, must be demonstrated using a tissue sample that on the one hand has clear morphological features of appropriate size and that is well described by classical histology.

In the present study, we combined readily available technologies to achieve 20- μ m lateral image resolution and to match this information to high quality optical microscopy images as they are used in the histological practice. Because of its highly complex anatomical features, we used the mammalian testis as a model to establish the complete work flow from the acquisition of MALDI images with lateral resolution near the single cell level, the proper match with histological information derived from standard optical microscopy, to the identification of proteins of interest using a top-down approach.

EXPERIMENTAL PROCEDURES

Chemicals—All chemicals were of the highest purity obtainable. Acetonitrile (ACN), ethanol, trifluoroacetic acid (TFA), formic acid, Tris, and reagents for H&E staining were purchased from Sigma-Aldrich. The MALDI matrix (α -cyano-4-hydroxycinnamic acid) was obtained from Bruker Daltonik GmbH (Bremen, Germany).

Rat Testis Tissue Preparation—Male Sprague-Dawley rats at adult stage maintained under standard care were used for tissue collection. They were purchased from Elevage Janvier (Le Genest-Saint-Isle, France). Animals were sacrificed by CO₂ gas and cervical dislocation. Testes were removed and washed with phosphate-buffered saline. Organs were then carefully wrapped in aluminum foil and progressively frozen by gently lowering the tissue into a liquid nitrogen tank. This procedure was accomplished in ~ 30 – 60 s to preserve the tissue shape and protect biological components from degradation. Samples were then stored at -80°C until required. All further movements of tissues were done on dry ice to minimize the possibility of localized tissue warming.

Tissue sections were prepared on a Leica CM 1900 UV cryostat (Leica Microsystems GmbH, Wetzlar, Germany) with the microtome chamber chilled at -22°C and the specimen holder at -12°C . Section 12- μ m thick were cut and thaw mounted onto ITO-coated microscopic slides (Bruker Daltonik GmbH) adapted for MALDI mass spectrometry. Following thaw mounting of tissue sections, MALDI target slides were allowed to dry for 1 h in a desiccator before washing and then were carefully washed in Coplin jars with no swirling. ITO slides were washed twice for 1 min each in 70% ethanol and then in 96% ethanol for 1 min. Following washing, ITO slides were tilted against paper towels to remove solvent and dried in a desiccator for 1 h before matrix deposition.

Matrix Coating—Matrix coating was performed using the ImagePrep device (Bruker Daltonik GmbH), spraying α -cyano-4-hydroxycinnamic acid matrix (7 mg/ml in 60:40 ACN/H₂O, 0.2% TFA) according to the manufacturer's standard protocol. In brief, a piezo-electric nebulizer is used to generate a fine mist of matrix solution droplets that create a homogeneous coverage of tissue sections by gravitational deposition (14). Following matrix application, slides were dipped twice in ice-cold 10 mM ammonium dihydrogen phosphate, 0.1% TFA solution.

MALDI Mass Spectrometry Imaging—MALDI mass spectra were acquired on an UltrafleXtreme MALDI-TOF/TOF instrument (Bruker Daltonik GmbH) equipped with a smartbeam II laser (Nd:YAG, 355 nm) at "minimum" focus setting. This second generation smartbeam laser provides a highly structured laser beam with a near flat top energy profile when averaged across a high number of laser shots and allows high sensitivity and lateral resolution at the same time (13, 15). Protein mass spectra were acquired from each spot in an automated fashion in linear positive ion mode and in the mass range of 2–30 kDa. Ions were detected in the 2–16-kDa range. Acceleration voltage was 25 kV, and deflection up to 1500 m/z was used to suppress matrix and other low molecular weight signals.

For image acquisition, a 20- μ m raster width was selected, and 200 individual spectra were acquired at 1000-Hz repetition rate and accumulated for each pixel. Spectra were processed by base-line correction and smoothing using FlexAnalysis 3.3 software (Bruker Daltonik GmbH). Image analysis and data visualization were performed with the FlexImaging 3.0 software (Bruker Daltonik GmbH).

Protein Identification—Whole rat testes were ground in liquid nitrogen, and the resulting powder was mechanically disrupted and homogenized with a Teflon pestle in 3 volumes of ice-cold 20 mM Tris lysis buffer, pH 7.5. The extract was homogenized by sonication on ice and centrifuged at $15,000 \times g$ for 30 min at 4°C . Supernatants were ultracentrifuged at $105,000 \times g$ for 1 h at 4°C and further fractionated on an Amicon Ultra 30,000 device (Millipore, Saint-Quentin-en-Yvelines, France) to collect protein fractions below 30 kDa. Protein concentration was determined using the bicinchoninic acid assay (Pierce). The fraction was further fractionated by RP-HPLC. Sample (2 mg), resuspended in 1 ml of solvent A (0.1% TFA in water, v/v) was loaded onto a C₁₈ RP-HPLC column (Vydac 218TP54; 4.6×150 -mm inner diameter; particle size, 5 μ m; Interchim, Montluçon, France) at a flow rate of 1 ml/min. Bound proteins were eluted with a linear gradient of 2–95% solvent B (95% ACN, 5% water containing 0.1% TFA, v/v) over a period of 90 min at a flow rate of 1 ml/min. Eluents were monitored by UV absorbance at 280 nm. Fractions of 1 ml were collected individually, lyophilized, and resuspended in 15 μ l of water with 0.1% formic acid. An aliquot of each fraction (1 μ l) was withdrawn, mixed with 7 mg/ml α -cyano-4-hydroxycinnamic acid in 60:40:0.2 (ACN/water/TFA) and analyzed by MALDI-MS on an AutoFlex III SmartBeam MALDI-TOF mass spectrometer (Bruker Daltonik GmbH). Fractions containing m/z of interest were further analyzed by top-down sequencing on an LTQ-Orbitrap XL instrument (Thermo Fisher Scientific, Courtaboeuf, France) using CID. Proteins were loaded onto a C₁₈ (PepMap, Dionex, LC Packings, Amsterdam, The Netherlands) trapping precolumn (5 mm \times 300- μ m inner diameter, 300-Å pore size, 5 μ m) and separated onto a C₁₈ (PepMap, Dionex, LC Packings) analytical column (15 cm \times 300- μ m inner diameter, 300-Å pore size, 5 μ m). Mobile phases A (0.1% formic acid in water) and B (0.1% formic acid in ACN) were delivered by an Ultimate 3000 nanoflow LC system (Dionex, LC Packings). Proteins were eluted with a linear gradient of 2–90% solvent B at a flow rate of 250 nl/min for 140 min (including column equilibration). Full-scan mass spectra were acquired with the Orbitrap mass spectrometer at 60,000 resolving power, and the four most intense peptides were automatically selected for CID MS/MS scans in parallel in the linear ion trap (LTQ). An ESI voltage of 1.5 kV was applied directly to the HPLC buffer using the liquid junction provided by the nanoelectrospray Ion Max source (Thermo Scientific). The ion transfer tube temperature was set to 200°C . Ion injection times were calculated for each spectrum to accumulate $1e6$ ions in the Orbitrap for full MS scans and 10,000 ions in the LTQ for MS/MS scans. Normalized collision energy was set to 35% with an activation time of 30 ms. The Xcalibur software (Thermo Scientific) was used to create the peak list from raw data. MS/MS spectra were searched against the Swiss-Prot

Database (release April 10, 2010; 514,789 sequences; 181,163,771 residues) filtered with the *Rattus norvegicus* taxonomy for protein identification using the Proteome Discoverer software (version 1.1.0.263) with the SEQUEST search algorithm. No enzyme selectivity was set. Oxidation of methionine; acetylation of lysine and the N-terminal residue; and phosphorylation of serine, threonine, and tyrosine were set as variable modifications. Mass tolerance for precursor ions and fragment ions was set to 10 ppm and 0.5 Da, respectively. Identified proteins were filtered based on Xcorr values for the corresponding charge state to obtain a false discovery rate of 1% (see supplemental Table 1).

Immunohistochemical Localization of Candidate Proteins—Immunohistochemical experiments were performed on Bouin solution-fixed and paraffin-embedded rat testes as described previously (16). Commercial rabbit polyclonal antibodies directed against synthetic peptides specific to thymosin β -4 (ab14335; Abcam) and thymosin β -10 (ab14338; Abcam) were both used at a dilution of 1:1000.

Histological Staining and Image Co-registration—After MALDI image acquisition, the matrix was washed off tissue sections in 70% ethanol, and a conventional H&E staining was performed (17). The stained slides were scanned using a MIRAX desk slide scanner (Carl Zeiss Microimaging, Jena, Germany). Both coarse and fine focus frequencies were set to 2, and the extended focus option was enabled. The MIRAX data set was aligned with the MALDI imaging data using the co-register image function of the software.

RESULTS

Laser Spot Diameter Is Crucial for Resolution—Twenty-micrometer-resolution imaging at high spectral intensity has not previously been achieved for proteins with standard nitrogen or solid state lasers with Gaussian beam profiles such as Nd:YAG lasers as the signal intensity suffers significant drops at small laser focus size of ~ 10 – $50\ \mu\text{m}$ (18–20). In this work, we used a second generation smartbeam II laser (15) with a structured beam profile (Fig. 1). For each shot, a structured pattern of very narrow Gaussian beam profiles on the 2–5- μm range is generated that is different for every shot. If several hundreds of shots are accumulated to generate a single pixel spectrum, in fact, a smartbeam laser delivers a gross flat top beam profile in stark contrast to standard Nd:YAG lasers with their Gaussian beam profile (Fig. 1A). Consequently, all spots within the ~ 10 – $20\text{-}\mu\text{m}$ laser focus of the smartbeam II are irradiated at identical fluence, providing steep edges contrary to the Gaussian laser beam that presents smooth flanks, and only a small fraction of the focus area can be used to MALDI analyze an image spot. Indeed, for the MALDI laser fluence distribution within a spot area, three different situations can be distinguished. 1) In the near-threshold irradiation area (Fig. 1A, in green), ions are generated efficiently and contribute greatly to the image brightness. 2) In the high irradiation area (Fig. 1A, in red), the sample is ablated quickly and contributes only a little to the ion signal. In addition, strong in-source decay of analytes (21) may result. 3) In the subthreshold irradiation area (Fig. 1A, in gray) in which analytes and matrix are desorbed, the energy of the MALDI process is not high enough to successfully ionize the analytes. Here, the surface is matrix-depleted without concomitant generation of ion intensity. The influence of laser beam profile on the ability to

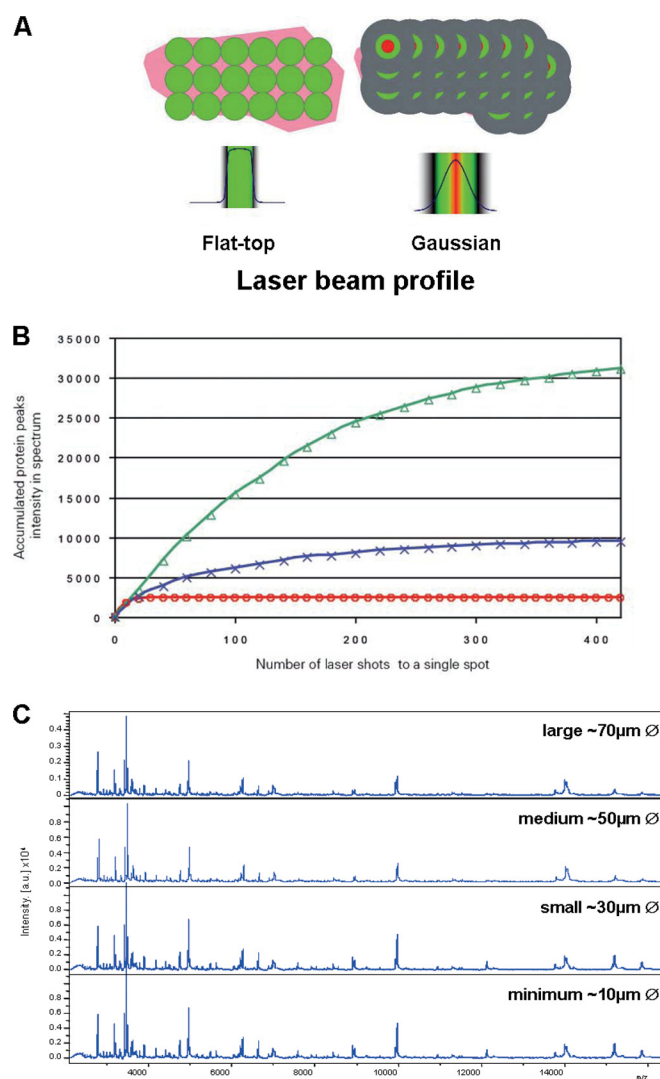


FIG. 1. Laser spot profile is crucial for image lateral resolution. A, beam profiles of the smartbeam laser and the Gaussian Nd:YAG laser. The color code for the different zones in the focus profile are as follows: near-laser threshold irradiation area with high MALDI ion abundance, green; high laser irradiation area with high sample ablation and low ion yield, red; and subthreshold laser irradiation area with matrix ablation without ion generation, gray. The imaging case shows a Gaussian profile with the same raster width at larger beam diameter, which represents the “oversampling” case discussed in the text. B, accumulated protein signal intensity as a function of the number of laser shots obtained with the smartbeam laser (green), Gaussian Nd:YAG laser (red), and N₂ laser (blue). C, mass spectra acquired directly from rat brain tissue with the smartbeam II laser with different focus diameters ranging from ~ 70 to $\sim 10\ \mu\text{m}$ (same number of laser shots). A significant loss of peak intensity is not observed across the tested focus range. &U2300, laser spot diameter; a.u., arbitrary units.

extract information from samples including tissue by MALDI is shown in Fig. 1B. In the case of the Gaussian profile-shaped Nd:YAG laser, the MALDI sample (ACTH CLIP-(18–39)) was ablated quickly and did not provide for any additional signal even after a low number of shots (~ 30 shots) on a given spot (Fig. 1B, in red plot). With an N₂ laser, the protein signal was

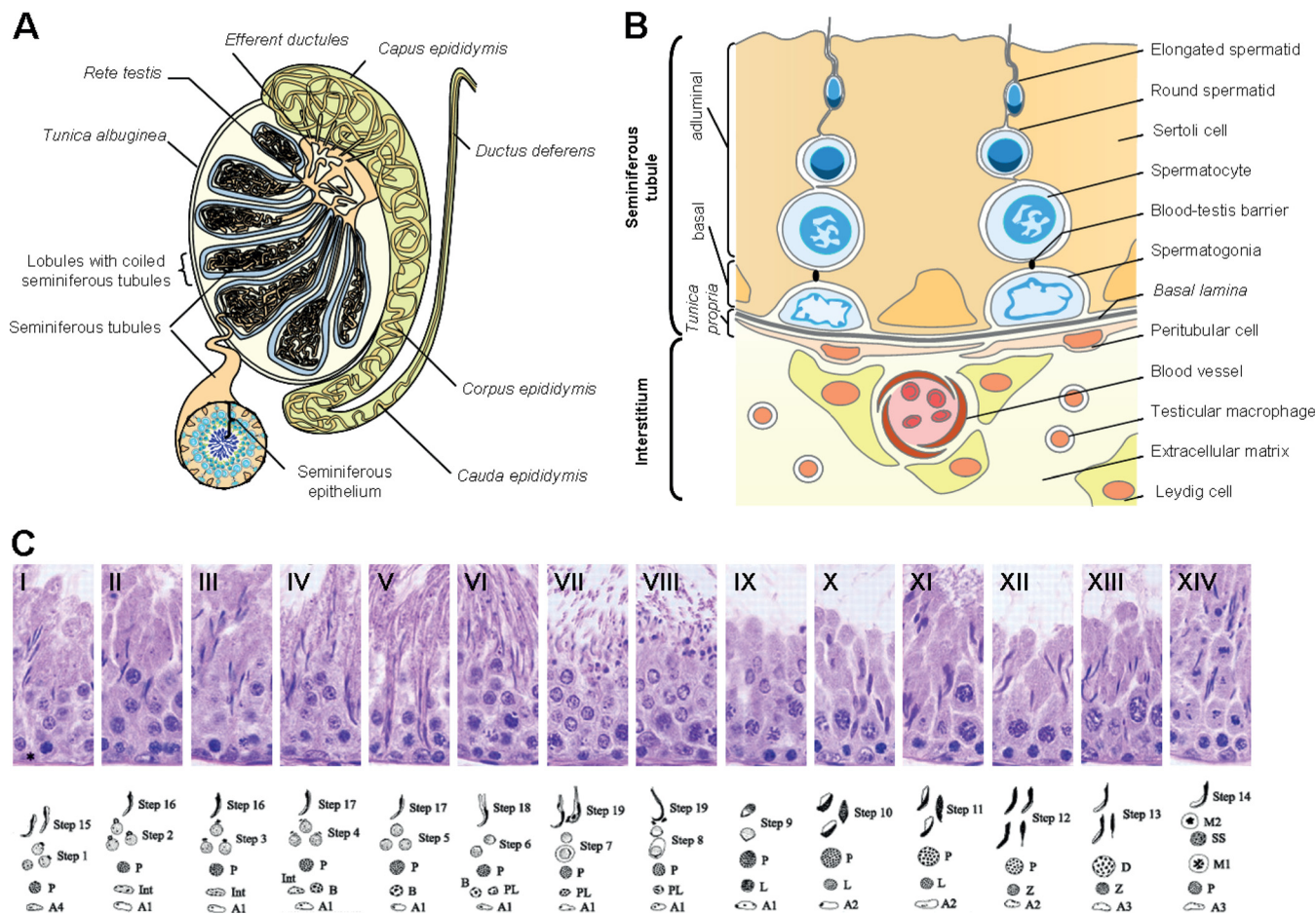


FIG. 2. A, schematic representation of the mammalian testis. Spermatozoa produced in the seminiferous tubules transit through the *rete testis* and efferent ducts to the epididymis in which they will be stored and matured before ejaculation. B, schematic close-up diagram of testicular anatomy. The interstitial compartment, which is highly vascularized, contains principally the testosterone-producing Leydig cells, fibroblasts, and macrophages. The seminiferous tubules, bounded by a basal membrane (*basal lamina*), contain the somatic Sertoli cells and the germ cells at various stages of their development. The black spots within the tubule indicate the tight junctions between Sertoli cells, which delimit the basal compartment. This compartment contains the spermatogonia and the newly formed primary spermatocytes, which are not shown in this representation. The adluminal compartment contains mature spermatocytes and spermatids. This diagram is not drawn to scale. C, cycle of the seminiferous epithelium in the rat (adapted from Ref. 55). Histological sections and schematic representations of the 14 stages (numbered from I to XIV) indicate all possible associations of germ cells that can be observed in tubules from a testis tissue section. This classification is essentially based on the morphogenesis of the acrosome of spermatids from the less differentiated step 1 to the highly differentiated step 19. The various types of spermatogonia (A1, A2, A3, A4, intermediate (Int), and B) and of spermatocytes (preleptotene (PL), leptotene (L), zygotene (Z), pachytene (P), diplotene (D), M1, and M2) are also represented.

observable much longer (~ 300 shots; Fig 1B, blue plot). The smartbeam II laser (Fig. 1B, in green plot) provided an even higher protein signal intensity over 400 shots at drastically lower fluence as compared with N_2 or Gaussian Nd:YAG lasers (15). Fig. 1A also explains why oversampling, *i.e.* the high resolution rastering of the sample using a less resolved Gaussian laser focus, does not provide bright and highly resolved images. The gray rings indicate the ablation of matrix and analyte subthreshold, and therefore, the area is inactivated in its contribution to the image brightness as discussed at greater detail in the literature (22, 23).

From mass spectra acquired on rat brain tissue, we observed that with the classic Nd:YAG laser increasing lateral resolution had a detrimental effect on the spectral quality

compared with the smartbeam II laser (data not shown) with which the mass spectral quality was preserved (Fig. 1C). Therefore, we used a setup with a smartbeam II laser focused to approximately 20 μm for the present study on the rat testis model.

Spermatogenesis in Rat, a Relevant Model for MALDI Imaging Development—For the purpose of this study, it is necessary to describe briefly the organization of spermatogenesis. Mammalian spermatogenesis takes place in the seminiferous tubules of the testis (Fig. 2, A and B). It is classically divided into three phases. In the first (proliferative or mitotic) phase, primitive germ cells (*i.e.* spermatogonia) undergo a series of mitotic divisions. In the second (meiotic) phase, spermatocytes undergo two consecutive divisions to

produce the haploid spermatids. In the third (spermiogenesis) phase, spermatids differentiate into spermatozoa.

An intriguing feature of spermatogenesis is that the developing germ cells form associations with fixed composition or stages, which constitute the cycle of the seminiferous epithelium (Fig. 2C). The fundamental organization and integrity of this epithelium are provided by the somatic Sertoli cells. In rats, classification of the seminiferous epithelium cycle by Leblond and Clermont (24) defines 14 stages (designated I–XIV) in which spermiogenesis, which refers to the morphological transformation of spermatids into spermatozoa, involves 19 differentiation steps (from 1 to 19) (Fig. 2C). This last step of germ cell development is a striking and unique example of cell differentiation involving acrosome formation, nuclear condensation, and flagellum biogenesis. Another intriguing feature of spermatogenesis is that there is a distinct ordering of cell associations along the length of the seminiferous tubules (segments) that has been called the “wave of the seminiferous epithelium” (25). Thus, a wave encompasses all 14 segments that are composed of various cell associations. A segment is a portion of seminiferous tubule in its longitudinal axis occupied by a single cell association or stage (Fig. 2C).

Assessing Protein Distribution in Seminiferous Tubules—To examine the distribution of proteins within specific regions of the seminiferous tubules, a transverse section of the testis of an adult rat stained with H&E (Fig. 3A) was superimposed with its corresponding molecular image generated at a 20- μm lateral resolution (Fig. 3, B, C, and D). The molecular images, reconstructed from a set of selected signals at m/z 4937, 5455, and 10,261 (Fig. 3C) and at m/z 4964, 5455, and 10,261 (Fig. 3D) showed a structure of concentric rings in only some of the seminiferous tubules. The latter corresponded to stages of the seminiferous epithelium at which late spermatids are about to be released into the lumen (spermiation) (stages VI–VIII). A second molecular image constructed from signals at m/z 2396 (in green) and m/z 3153 (in red) clearly identifies a blood vessel and seminiferous tubules containing early and elongating spermatids up to step 17, respectively (Fig. 3B).

MALDI Imaging at 20 μm , a Breakthrough for Histological Evaluation—High resolution images were used to further examine the distribution of proteins at the cellular level within the seminiferous tubules. A closer evaluation of the sections stained with H&E after the MALDI imaging experiment was possible because of the high image quality. It is of particular importance that, even after irradiating the tissue with a high number of laser shots, the tissue is not altered in its morphology. This is due to the low laser fluence that can be used with the smartbeam II beam pattern. At 20- μm lateral resolution, molecular signals could be matched with a highly specific area within the seminiferous tubules corresponding to germ cells at different stages of their development (Fig. 4). In a seminiferous tubule section corresponding to stage VII of the seminiferous epithelium classification, the proteins corre-

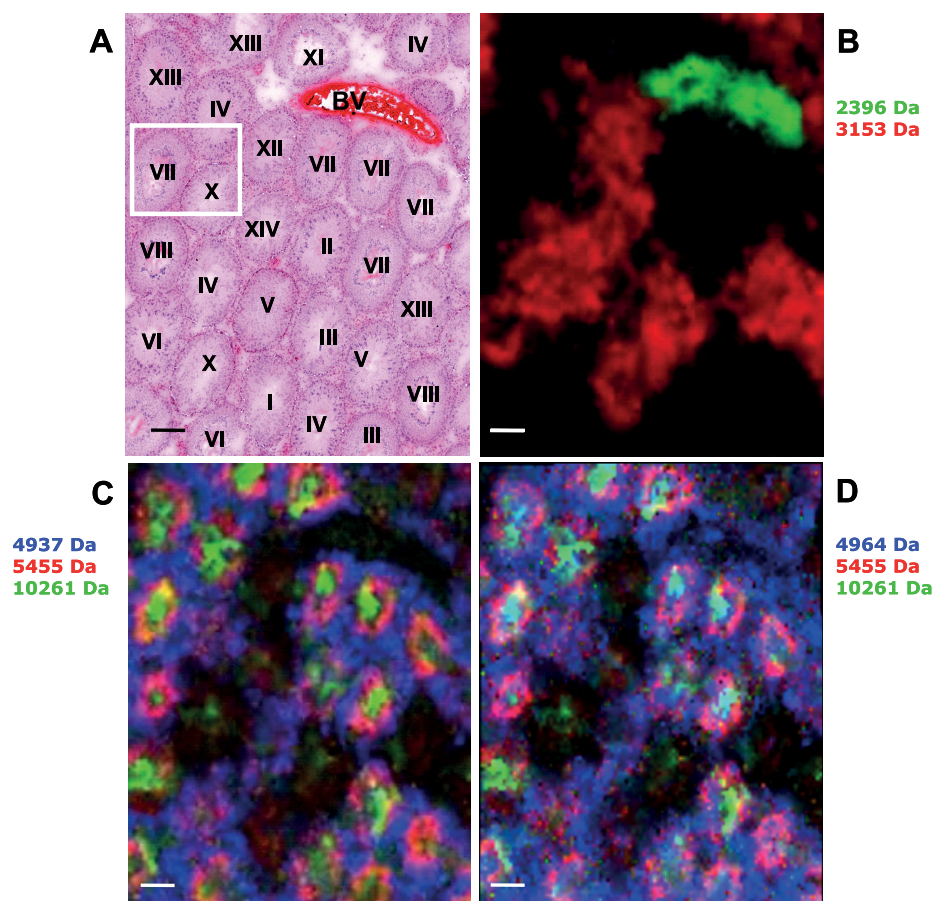
sponding to m/z 4937 and 4964, displaying a similar distribution, could be assigned to the periphery of the tubule section where spermatogonia and preleptotene and pachytene spermatocytes are present (Fig. 4, A and B). The m/z 5455 could be assigned to the adluminal compartment where early and elongating spermatids are present (Fig. 4, A and B). Finally, the signal at 10,261 Da was exclusively evidenced in lumina in which flagellae from step 18–19 spermatids were present (Fig. 4, A and B). In a tubule section at stage X of the seminiferous epithelium classification that only contained spermatids at an early differentiation step (*i.e.* step 10), no signal was observed for molecular species at 5,455 and 10,261 Da (Fig. 4, A and B). Careful examination of H&E and molecular images allowed us to superimpose the *in situ* localization of selected masses onto the map of spermatogenesis from Leblond and Clermont (24) as modified by Dym and Clermont (26) (Fig. 4C).

Work Flow for Identification of Candidate Proteins—*In situ* identification of proteins corresponding to m/z detected by IMS is still challenging. Thus, an identification procedure based on the extraction of proteins from whole rat testis was developed (Fig. 5A) that led to the identification of the full-length thymosin β -10 (UniProt accession number P63312; average $\text{MH}^+ = 4937.5$ Da) and thymosin β -4 (UniProt accession number P62329; average $\text{MH}^+ = 4964.5$ Da) proteins (Fig. 5B) and to a fragment of long-chain-fatty-acid-CoA ligase (ACSL-(19–48); UniProt accession number Q924N5; average $\text{MH}^+ = 3153.2$ Da) (supplemental Fig. 1).

Thymosins β -4 (TYB4_RAT) and β -10 (TYB10_RAT) were identified as singly acetylated protein species matching the IMS results by 0.5 Da (supplemental Table 1). The MS/MS spectra are provided for the localization of the acetyl groups at Lys-3 for both thymosins. Identifications unequivocally corresponded to average masses detected in IMS at m/z 4937, 4964, and 3153, respectively (supplemental Table 1).

Validation of Molecular Imaging Data by Immunohistochemistry—For validation of the MALDI imaging data obtained at 20- μm resolution, we selected two of the identified proteins for which a good quality commercial antibody was available (*i.e.* thymosin β -4 and thymosin β -10). Immunohistochemical studies performed on adult rat testis sections revealed that thymosin β -4 and thymosin β -10 were expressed in a stage-dependent manner in the seminiferous tubules (Fig. 6, A and B, respectively). Signal was also detected for both proteins in the interstitial compartment (Fig. 6, A and B). A transverse testis section at higher magnification showed a strong labeling for thymosin β -4 at the periphery of the tubules, corresponding to the cytoplasm of preleptotene and pachytene spermatocytes (Fig. 6C). A staining with much lower intensity was also visible in the cytoplasm of early spermatids (Fig. 6C). Thymosin β -10 was also strongly localized in the cytoplasm of pachytene spermatocytes and to a lesser extent in the cytoplasm of early spermatids (Fig. 6D). Interestingly, immunoreactivity for both thymosins β -4 and β -10 was observed in the cytoplasm of elongated spermatids and into the residual

FIG. 3. Assessing protein distribution in seminiferous tubules. *A*, a transverse section of the testis of an adult rat stained with hematoxylin and eosin. *Roman numerals* indicate stages of the seminiferous epithelial cycle in rat species by Leblond and Clermont (24). The *white square* corresponds to the magnified section displayed in Fig. 4*A*. *BV*, blood vessel. *Scale bar*, 200 μm . *B*, molecular image reconstructed from selected masses shows a specific signal at *m/z* 2396 in a blood vessel (*green*), whereas *m/z* 3153 (*red*) is found in seminiferous tubules sections that do not contain step 18–19 spermatids. *Scale bar*, 200 μm . *C* and *D*, molecular images reconstructed from selected protein ions of *m/z* 4937, 5455, and 10,261 (*C*) and *m/z* 4964, 5455, and 10,261 (*D*) both show a structure of concentric rings in seminiferous tubules at specific stages of the seminiferous epithelium that contain late and elongated spermatids. *Scale bar*, 200 μm .



bodies, corresponding to the portion of cytoplasm of elongated spermatids shed at the time of spermiation (Fig. 6, *A* and *B*).

DISCUSSION

MALDI imaging is emerging as a powerful tool for investigating the distribution of biomolecules in thin tissue sections by direct, top-down, label-free profiling. Over the past 2 years, a significant number of studies have demonstrated the ability of MALDI imaging to localize and identify protein markers or fragments of larger predecessor proteins that classify tissue in terms of health state in particular for cancers. As an example, the Reg α fragment of the 11 S proteasome activator complex was identified as a novel biomarker candidate for ovary cancers (2). More recently, a fragment of mitogen-activated protein kinase/extracellular signal-regulated kinase kinase 2 (MEKK2) was shown to discriminate prostate cancer from uninvolved tissues (5). The full 8.4-kDa cysteine-rich intestinal protein 1 (CRIP1) was identified to be one in a panel of markers distinguishing HER2-positive from HER2-negative breast cancers (6). Panels of such biomarkers showed good specificities and sensitivities for assigning the health states and possibly support histopathological work in the clinic in the near future. However, typically, these analyses were performed with low image resolutions (*i.e.* 100–200 μm) that could not be clearly

correlated with tissue morphology at the light microscopic level typically utilized by histologists and pathologists.

Over the past decade, the increase of lateral resolution in imaging mass spectrometry has been the focus of great attention (27). The methods used to increase image resolution ranged from expanding the cellular distances by sample stretching (28–30) to improving matrix application protocols (14, 31–35). Alternatively, ion microscopic instrumentation was also used (19, 36). Suitable sample preparation with attempts to improve protein signals and avoid delocalization and degradation (37–39) and proper matrix selection and application present a critical technical issue to obtain high resolution image quality (8). Various instruments have been designed to enable standardized matrix deposition and to optimize preparation conditions, a prerequisite for sensitivity enhancement and improvement of lateral resolution (35, 40). Most limitations regarding matrix application have been tackled with the development of a vibrational vaporization instrument, which allows controlling the degree of tissue wetting during matrix application and avoids diffusion by controlled drying. In addition, the instrument allows the control of matrix crystal size and homogeneity of the matrix layer to optimize efficient analyte extraction and the reproducible quality of mass images (8).

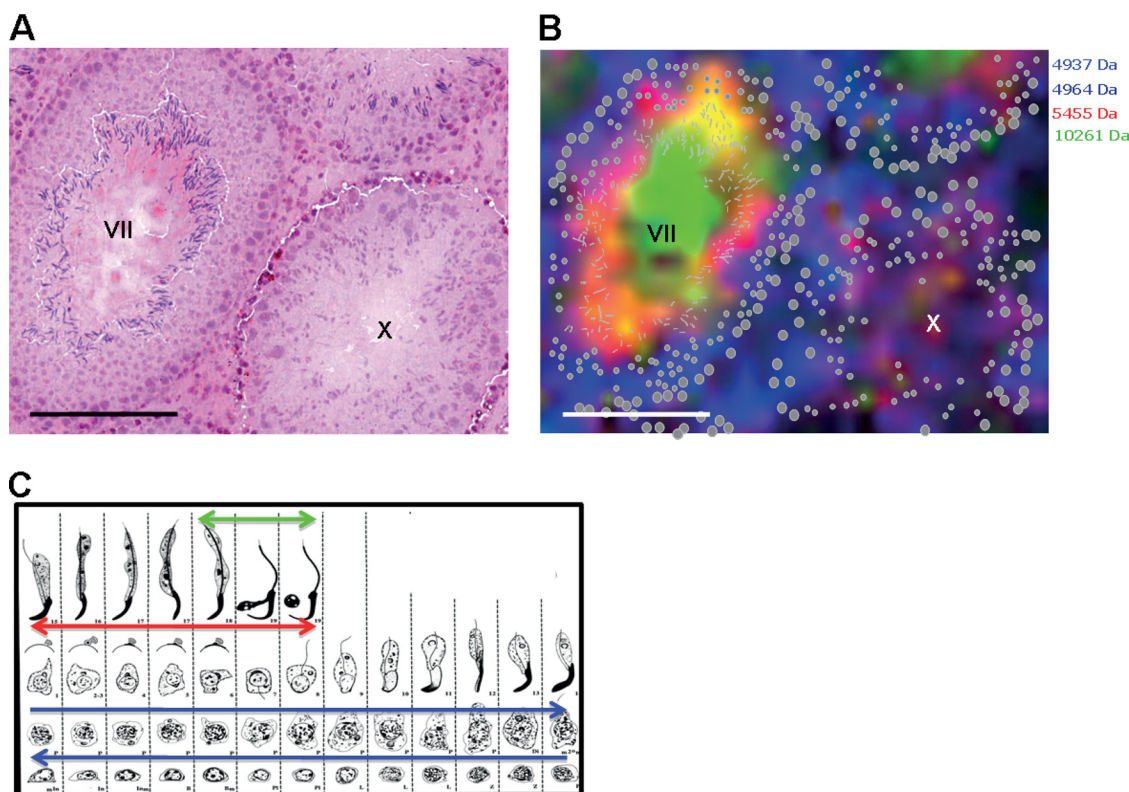


FIG. 4. Correlation between histology and molecular imaging at high resolution. Two seminiferous tubule sections are displayed that correspond to stage VII and stage X of the seminiferous epithelium classification. **A**, close-up of a transverse section of the testis of an adult rat stained with hematoxylin and eosin. Scale bar, 200 μm . **B**, corresponding molecular image at a 20- μm lateral resolution. Four proteins in the stage VII section corresponding to m/z 4937, 4964, 5455, and 10,261 could be assigned, respectively, to the basal compartment, (m/z 4937 and 4964) the adluminal compartment (m/z 5455), and the lumen (m/z 10,261). The signal at m/z 10,261 can be matched with the presence of flagellae from step 18–19 spermatids. In the stage X section, which contains spermatids at early differentiation steps (step 10), no signal was observed for molecular species at m/z 5455 and 10,261. In **C**, the lower panel shows summaries of the *in situ* localization of selected masses superimposed on the map of spermatogenesis reprinted with permission from Leblond and Clermont (24) as modified by Dym and Clermont (26). Scale bar, 200 μm .

To date, only three groups, on customized instruments, have addressed the effect of laser spot diameter on MALDI imaging lateral resolution. A modified scanning laser microprobe instrument achieved a lateral resolution around 1 μm for low mass ions ($m/z < 5000$) (27). More recently, a scanning MALDI-TOF instrument equipped with a coaxial laser illumination ion source was developed that allowed proteins up to 27 kDa to be detected with a lateral resolution of 7 μm (19). Interestingly, a MALDI mass spectrometer using magnifying ion optics configured like an ion microscope was developed to reconstruct 4- μm -resolution images from 200- μm irradiated areas without sensitivity losses (36). However, only a few analyte images could be analyzed in MALDI images with this instrumental design.

Using conventional MALDI-TOF instruments, an alternative approach based on oversampling was used to record images with a pixel size 4 times smaller than that of the laser spot (22, 23). Oversampling refers to incremental movement of the laser spot across the sample in steps smaller than the laser focus size. However, improved image resolution from tissues thus leads to a loss in spectral quality and a major reduction in MALDI image brightness because the amount of analyte spe-

cific to each increment is reduced. Theoretically, the resolution achievable by oversampling is only limited by the ability to precisely control movement of the sample stage, but in practice, it appears to be limited to roughly half the laser spot diameter (20). This effect is most pronounced with standard Nd:YAG lasers because of the low fluence margin of the beam profile (Fig. 1). Finally, it is also worth noting that the lateral resolution in an IMS analysis also depends on the mass spectrometer hardware including laser type and focus, step movements of the sample stage, and instrument sensitivity. Very dry sample preparation (to forestall diffusion), oversampling, and too small laser diameters ($< \sim 10 \mu\text{m}$) effectively reduce analyte yield per image pixel. As a result, most high resolution MALDI images are acquired on abundant and easily extracted analytes such as plasma membrane phospholipids (41). Acquiring bright and well resolved IMS data from peptides and proteins > 2000 Da represents a considerably higher challenge.

Flat top laser beam profiles are theoretically ideal for imaging as they homogeneously produce ions across the entire laser spot and have no flanks. The present work demonstrates that efficient acquisition of adjacent image pixels at the size of

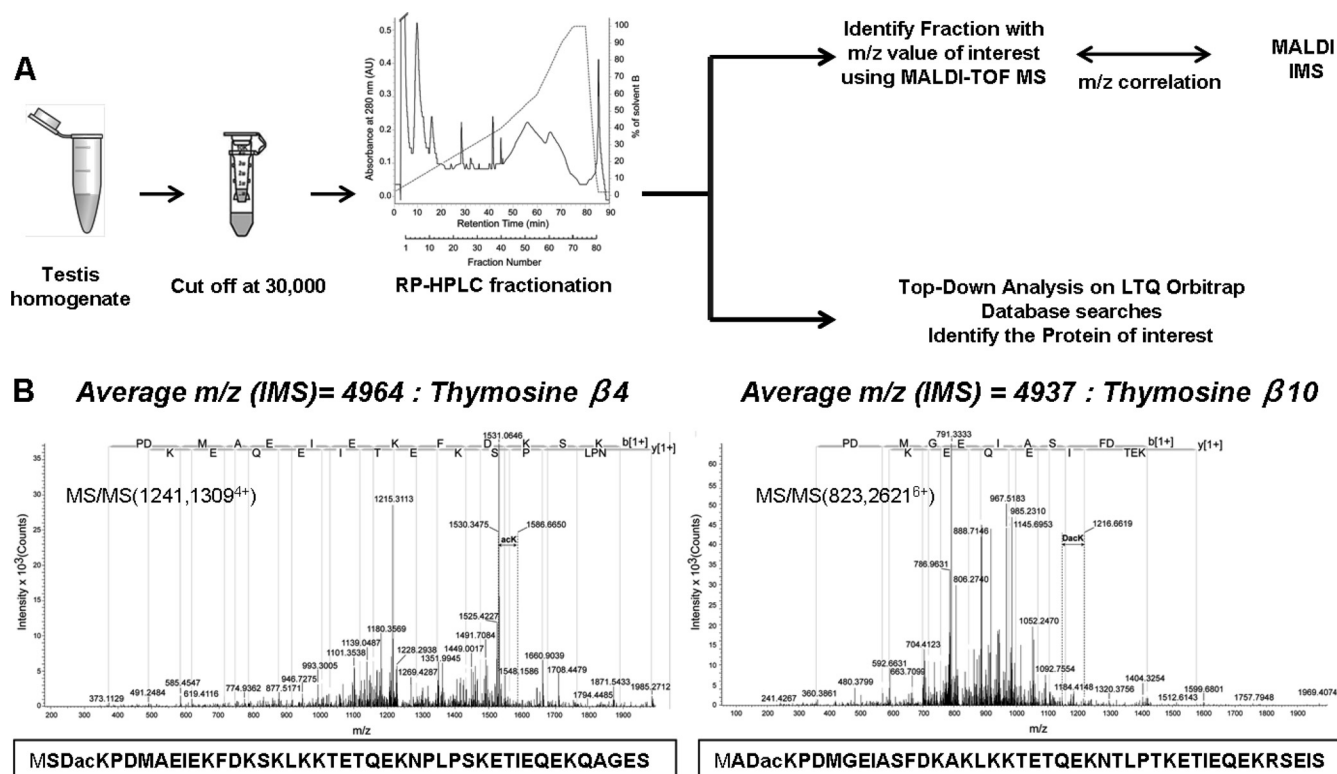


FIG. 5. Protein identification work flow. A, protein extraction was performed on whole rat testis. Extracts were then filtered on the ultrafiltrate fraction below 30 kDa. Filtrate was separated by RP-HPLC. Fractions were collected and first spotted onto a MALDI target to select the fraction containing the m/z observed by IMS. Selected fractions were then analyzed by top-down nano-ESI tandem mass spectrometry. B, nano-ESI-LTQ-Orbitrap MS/MS profiles of the monoisotopic ion precursor m/z 1241.1309 $^{4+}$ ($MH^+ = 4961.5021$) corresponding to the average m/z 4964 observed by IMS (left) and monoisotopic ion precursor m/z 823.2621 $^{6+}$ ($MH^+ = 4934.5365$) corresponding to the average m/z 4937 observed by IMS (right). Sequences obtained show 97.73% sequence identity with thymosin β -4 (with acetylated Lys-3) and thymosin β -10 (with acetylated Lys-3).

the laser spot is possible with a lower laser fluence that does not destroy the tissue (Fig. 1A). This is a prerequisite for a histopathological imaging work flow in which the MALDI image is acquired first and followed by H&E staining and microscopic analysis on the same tissue section.

The only way to assess the resolving power of a MALDI imaging experiment is to analyze biological tissue displaying anatomical features that are of the right order of magnitude. Experiments on artificial structures such as grids, felt pen markings, and the like cannot be extrapolated to real tissues because the effect of the sample preparation and crystallization cannot be assessed. Also, on real tissue, a significantly higher laser fluence may be needed, possibly requiring laser focus settings well above technical limits. We introduce the rat testis, in particular its seminiferous epithelium, as a highly relevant model to evaluate MALDI imaging of proteins at 20- μ m lateral resolution (Fig. 2).

Spermatogenesis is a sophisticated process facilitating transmission of the genetic patrimony and, thus, perpetuation of the species. The process features the germ cell-specific events associated with meiosis as well as certain unique events related to chromatin remodeling, repackaging, and transcriptional reprogramming. Moreover, spermatozoa bear hyperselected traits associated with shape and energy pro-

duction as well as enhanced flagellum development. Control of this unique differentiation incorporates juxtacrine, paracrine, and endocrine factor information and is conditioned by the successive activation and/or repression of thousands of genes and proteins including numerous testis-specific isoforms modulating somatic and germ cell activity (for reviews, see Refs. 42–45). The communication network linking the various cellular activities during spermatogenesis is highly complex and sophisticated (46, 47). All these features contribute to make the testis, together with the brain, one of the most complex tissues in the body. Unraveling aspects of this complexity using cell culturing approaches has always been problematic because of difficulties in culturing more differentiated male germ cell types. The absence of this “testing ground” places greater emphasis on quality omics analysis in advance of *in vivo* testing of hypotheses. Indeed, over the past 10 years, advances in genomics and postgenomics have improved our knowledge of spermatogenesis by identifying numerous genes and proteins essential for the development of functional male gametes (for a review, see Ref. 48). In such a context, MALDI imaging now appears to be an incredibly seductive technology as monitoring germ cell protein expression directly within the seminiferous tubules yet seems feasible.

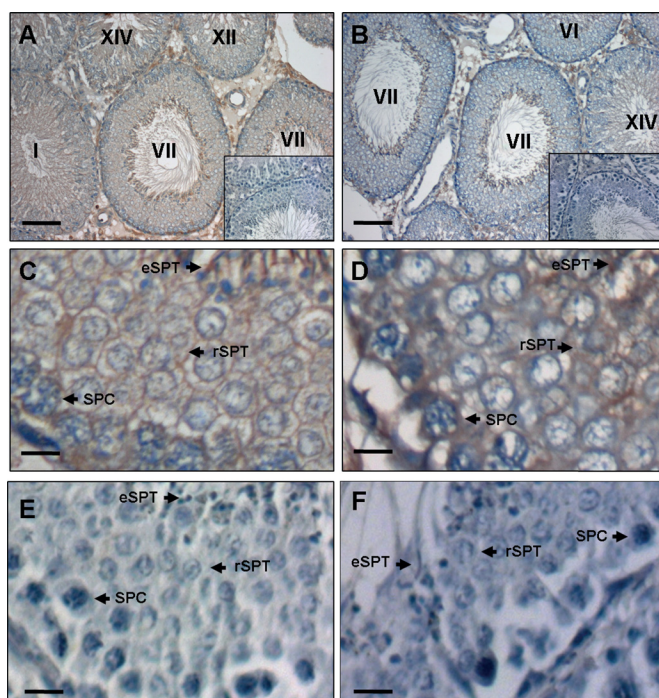


FIG. 6. Immunolocalization of thymosin β -4 and thymosin β -10 in adult rat testis. Organs were fixed by immersion in Bouin's fixative solution. Thymosin β -4 and thymosin β -10 were detected with specific rabbit polyclonal antisera raised against synthetic peptides as described under "Experimental Procedures." Experiments were carried out on serial rat testis sections. *Roman numerals* indicate the stages of the seminiferous epithelium. *A*, scale bar, 200 μm . A stage-dependent thymosin β -4 labeling is distributed within the seminiferous epithelium. Immunoreactivity is also seen throughout the interstitium. *B*, scale bar, 200 μm . A stage-dependent thymosin β -10 labeling is distributed within the seminiferous epithelium. Immunoreactivity is also visible in the interstitial space. *C*, thymosin β -4 immunoreactivity is first detected during stage VII in the cytoplasm of pachytene spermatocytes (SPC) and to a lower extent in that of round spermatids (rSPT). Staining is also concentrated near the head of elongated spermatids (eSPT). Scale bar, 20 μm . *D*, at stage VII, thymosin β -10 is strongly expressed in the cytoplasm of spermatocytes at the pachytene stage (SPC) and in that of round spermatids (rSPT). Staining is also visible in the cytoplasm of elongated spermatids (eSPT). The specificity of the immunoreaction was ascertained by parallel experiments in which primary antibodies were omitted (*A* and *B*, insets, and *E* and *F*). *E*, thymosin β -4 negative control experiment. Scale bar, 20 μm . *F*, thymosin β -10 negative control experiment. Scale bar, 20 μm .

In the present study, we demonstrated that a set of proteins expressed at various germ cell developmental stages can be visualized *in situ* without disturbing the cellular architecture of the seminiferous tubules (Figs. 3 and 4). At 20- μm lateral resolution (Fig. 4), these selected m/z values could be assigned to premeiotic and meiotic germ cells (*i.e.* m/z 4937 and m/z 4964) and to postmeiotic haploid spermatids at various steps of spermiogenesis (*i.e.* m/z 5455) (Fig. 4). Interestingly, a careful examination of both histological and molecular images suggests that m/z 5455 could be specifically associated with the developing head/acrosome of spermatids (Fig. 4). Additionally, histological examination also indicated that the

m/z 10,261 can be associated with the flagella of spermatids at the time of spermiation (Fig. 4). MALDI imaging at 20 μm thus appears to be a very powerful tool to tackle *in situ* protein expression (and further identification) in tissues with complex anatomical features.

Using a top-down tissue protein marker identification workflow, we established that the ions m/z 4937 and 4964 derived from tissue correspond to thymosin β -10 and thymosin β -4, respectively. These actin-sequestering proteins are closely related in structure and are present in many tissues (49). In the testis, thymosin β -10 is expressed in the germ cell lineage from pachytene spermatocytes to postmeiotic haploid spermatids and is known to be involved in spermatid development (50). This result is in accordance with the molecular image of m/z 4937 ion, which is predominant at the periphery of the tubules. The present work provides the first unambiguous evidence of thymosin β -4 expression within the testis. Again, the presence of the m/z 4964 ion at the periphery of the seminiferous tubules matches the strong immunoreactive signal observed for thymosin β -4 in spermatocytes. For both proteins, the weaker immunoreactive signal evidenced in spermatids could not be superimposed with the corresponding molecular image. This probably corresponds to the sensitivity limit of IMS and to ionization competition with more abundant co-localized proteins. Interestingly, for both proteins, an immunoreactive signal was visible in the cytoplasm of elongated spermatids and most particularly into the residual bodies. These structures, measuring 1–2 μm are spread around the tubule lumen prior spermiation (stage VII). Signals for m/z 4937 and 4964 ions are most probably too diluted to be detectable at 20- μm lateral resolution.

Thymosin β -4 identified in our study is the precursor of the tetrapeptide *N*-acetyl-seryl-aspartyl-lysyl-proline (AcSDKP; 487 Da), a physiological negative regulator of hematopoietic stem cell proliferation (51). Expression of AcSDKP at very high levels was demonstrated by our laboratory in the rat testis (52). According to this previous study, AcSDKP is produced by interstitial cells (*i.e.* Leydig cells and testicular macrophages) and promotes spermatogonial survival. Interestingly, its presence in elongated spermatids, together with that of thymosin β -4, indicates that this peptide plays a role yet to be elucidated in the regulation of other steps of spermatogenesis (52). However, the biochemical details of Lys-3 deacetylation and N-terminal acetylation in AcSDKP remain unclear, although our data indicate that these reactions need to occur during AcSDKP processing.

In this study, we also identified a fragment (residues 19–48) of long-chain-fatty-acid-CoA ligase (ACSL-(19–48)) that corresponds to the m/z 3153 ion. The corresponding 79-kDa cytoplasmic progenitor protein is expressed in rodent gonads and brain. In the testis, it may participate in steroidogenesis and, through the multiple functions of acyl-CoA, in the regulation of the male gonad (53). This is another example for the ability of the top-down imaging strategy to specifically detect and identify

processed protein fragments including the definition of N and C termini (2, 5), which is difficult to achieve with bottom-up approaches. Unfortunately, the validation of molecular images by immunohistochemistry was not possible here due to the lack of good antibody against the protein (fragment). However, our IMS data suggest ACSL-(19–48) to be present at the periphery of seminiferous tubules. This is in accordance with previous work showing that the protein is expressed in Leydig cells and to a lesser extent in Sertoli cells and spermatogonia (53). In the rat testis, Leydig cells are isolated or clustered into small groups throughout the interstitial compartment. This probably leads to a signal dilution, explaining why m/z 3153 remained undetected even at 20- μ m lateral resolution.

In the present study, we demonstrated that the smartbeam II laser is a major improvement in the field of MALDI imaging with two key properties: the adjustable laser focus and the fact that minimizing the focus has no detrimental effect on the spectral quality. High resolution imaging on tissue sections down to the size of an individual cell (≤ 10 μ m) is a key issue to increase MALDI-IMS applicability in biological and biomedical research. The acquisition of high resolution molecular images primarily depends upon an appropriate laser spot diameter and a matrix application method that precludes analyte delocalization. As discussed above, only a few customized instruments are now capable of acquiring images at cellular length scales (≤ 10 μ m) (19, 27, 36). Interestingly, current limitations on laser spot size may be partially compensated for by using an oversampling approach (22). Still, matrix coating on tissue sections can be largely improved especially through optimization of matrix deposition steps and the production of submicron crystals such as those obtained by sieving (41) or sublimation (54). Further developments in this field are ongoing in our laboratory using the rat testis model to achieve a routine 10- μ m lateral resolution on a commercial instrument.

The results shown here prove that it is now possible to acquire MALDI images of proteins in the 10-kDa range at 20- μ m lateral resolution. The rat testis was used as a relevant model to demonstrate that this real resolution corresponded to complex anatomical features at the cellular level. The correlation of molecular signals was successfully established with the development of germ cells within the seminiferous epithelium. Indeed, the identification of ions in the testis images evidenced in this study is ongoing in our laboratory. In conclusion, our work clearly shows that high lateral resolution in MALDI imaging yet allows unambiguous correlation with histoanatomical and cytological microscopic images. This is a major step toward clinical applicability of IMS. Of interest from a methodological aspect is how much structural detail can result from the top-down imaging strategy if recombined with a top-down sequencing strategy (6) such as for thymosin acetylation and the proteolytic ACSL processing in this work.

Acknowledgments—We thank Dr. P. Calvel for the gift of testis drawings and Dr. Armin Holle (Bruker Daltonik GmbH) for careful reading of the manuscript.

* This work was supported in part by Biogenouest and by Infrastructures en Biologie Sante et Agronomie, Fonds Européen de Développement Régional, and Conseil Régional de Bretagne grants.

§ This article contains [supplemental Table 1](#) and [Fig. 1](#).

§ Both authors made equal contributions to this work.

¶ Holds a postdoctoral fellowship from Contrat de Projets Etat-Région Bretagne.

‡ Supported by the Bundesministerium für Bildung und Forschung (BMBF) (SYStems Biology TECHnologies (SYSTEC) Grant 0315508C; multimodal imaging of single cells: biomedical systems biology of tissues) and the Deutsche Forschungsgemeinschaft (SFB Grant 824, Z2).

§§ Supported by the BMBF (SYSTEC Grant 0315508C; multimodal imaging of single cells: biomedical systems biology of tissues).

¶¶ To whom correspondence should be addressed: INSERM U625, Proteomics Core Facility Biogenouest, Campus de Beaulieu, 35042 Rennes Cedex, France. Tel.: 33-2-2323-5279; Fax: 33-2-2323-5282; E-mail: charles.pineau@rennes.inserm.fr.

REFERENCES

1. Groseclose, M. R., Andersson, M., Hardesty, W. M., and Caprioli, R. M. (2007) Identification of proteins directly from tissue: in situ tryptic digestions coupled with imaging mass spectrometry. *J. Mass. Spectrom.* **42**, 254–262
2. Lemaire, R., Menguellet, S. A., Stauber, J., Marchaudon, V., Lucot, J. P., Collinet, P., Farine, M. O., Vinatier, D., Day, R., Ducoroy, P., Salzert, M., and Fournier, I. (2007) Specific MALDI imaging and profiling for biomarker hunting and validation: fragment of the 11S proteasome activator complex, Reg alpha fragment, is a new potential ovary cancer biomarker. *J. Proteome. Res.* **6**, 4127–4134
3. Minerva, L., Clerens, S., Baggerman, G., and Arckens, L. (2008) Direct profiling and identification of peptide expression differences in the pancreas of control and ob/ob mice by imaging mass spectrometry. *Proteomics* **8**, 3763–3774
4. Stauber, J., MacAleese, L., Franck, J., Claude, E., Snel, M., Kaletas, B. K., Wiel, I. M., Wisztorski, M., Fournier, I., and Heeren, R. M. (2010) On-tissue protein identification and imaging by MALDI-ion mobility mass spectrometry. *J. Am. Soc. Mass Spectrom.* **21**, 338–347
5. Cazares, L. H., Troyer, D., Mendinos, S., Lance, R. A., Nyalwidhe, J. O., Beydoun, H. A., Clements, M. A., Drake, R. R., and Semmes, O. J. (2009) Imaging mass spectrometry of a specific fragment of mitogen-activated protein kinase/extracellular signal-regulated kinase kinase 2 discriminates cancer from uninvolved prostate tissue. *Clin. Cancer Res.* **15**, 5541–5551
6. Rauser, S., Marquardt, C., Balluff, B., Deininger, S. O., Albers, C., Belau, E., Hartmer, R., Suckau, D., Specht, K., Ebert, M. P., Schmitt, M., Aubele, M., Höfler, H., and Walch, A. (2010) Classification of HER2 receptor status in breast cancer tissues by MALDI imaging mass spectrometry. *J. Proteome Res.* **9**, 1854–1863
7. Chaurand, P., Cornett, D. S., and Caprioli, R. M. (2006) Molecular imaging of thin mammalian tissue sections by mass spectrometry. *Curr. Opin. Biotechnol.* **17**, 431–436
8. MacAleese, L., Stauber, J., and Heeren, R. M. (2009) Perspectives for imaging mass spectrometry in the proteomics landscape. *Proteomics* **9**, 819–834
9. Heeren, R. M., Smith, D. F., Stauber, J., Kükler-Kaletas, B., and MacAleese, L. (2009) Imaging mass spectrometry: hype or hope? *J. Am. Soc. Mass Spectrom.* **20**, 1006–1014
10. Limon, A., Reyes-Ruiz, J. M., Eusebi, F., and Miledi, R. (2007) Properties of GluR3 receptors tagged with GFP at the amino or carboxyl terminus. *Proc. Natl. Acad. Sci. U.S.A.* **104**, 15526–15530
11. Farias-Eisner, R., and Reddy, S. T. (2010) Biomarkers for early detection of ovarian cancer. U. S. Patent **7**, 670,792
12. Campbell, L. L., and Polyak, K. (2007) Breast tumor heterogeneity: cancer stem cells or clonal evolution? *Cell Cycle* **6**, 2332–2338

13. Qiao, H., Spicer, V., and Ens, W. (2008) The effect of laser profile, fluence, and spot size on sensitivity in orthogonal-injection matrix-assisted laser desorption/ionization time-of-flight mass spectrometry. *Rapid Commun. Mass Spectrom.* **22**, 2779–2790
14. Schürenberg, M., and Deininger, S. (2010) Matrix application with ImagePrep, in *Imaging Mass Spectrometry: Protocols for Mass Microscopy* (Setou, M., ed) pp. 87–91, Springer, New York
15. Holle, A., Haase, A., Kayser, M., and Höhndorf, J. (2006) Optimizing UV laser focus profiles for improved MALDI performance. *J. Mass Spectrom.* **41**, 705–716
16. Com, E., Rolland, A. D., Guerrois, M., Aubry, F., Jégou, B., Vallet-Erdtmann, V., and Pineau, C. (2006) Identification, molecular cloning, and cellular distribution of the rat homolog of minichromosome maintenance protein 7 (MCM7) in the rat testis. *Mol. Reprod. Dev.* **73**, 866–877
17. Schwamborn, K., Krieg, R. C., Reska, M., Jakse, G., Knuechel, R., and Wellmann, A. (2007) Identifying prostate carcinoma by MALDI-Imaging. *Int. J. Mol. Med.* **20**, 155–159
18. Koestler, M., Kirsch, D., Hester, A., Leisner, A., Guenther, S., and Spengler, B. (2008) A high-resolution scanning microprobe matrix-assisted laser desorption/ionization ion source for imaging analysis on an ion trap/Fourier transform ion cyclotron resonance mass spectrometer. *Rapid Commun. Mass Spectrom.* **22**, 3275–3285
19. Chaurand, P., Schriver, K. E., and Caprioli, R. M. (2007) Instrument design and characterization for high resolution MALDI-MS imaging of tissue sections. *J. Mass Spectrom.* **42**, 476–489
20. McDonnell, L. A., and Heeren, R. M. (2007) Imaging mass spectrometry. *Mass Spectrom. Rev.* **26**, 606–643
21. Suckau, D., Resemann, A., Schuerenberg, M., Hufnagel, P., Franzen, J., and Holle, A. (2003) A novel MALDI LIFT-TOF/TOF mass spectrometer for proteomics. *Anal. Bioanal. Chem.* **376**, 952–965
22. Jurchen, J. C., Rubakhin, S. S., and Sweedler, J. V. (2005) MALDI-MS imaging of features smaller than the size of the laser beam. *J. Am. Soc. Mass Spectrom.* **16**, 1654–1659
23. Li, Y., Shrestha, B., and Vertes, A. (2007) Atmospheric pressure molecular imaging by infrared MALDI mass spectrometry. *Anal. Chem.* **79**, 523–532
24. Leblond, C. P., and Clermont, Y. (1952) Definition of stages of the cycle of the seminiferous epithelium in the rat. *Ann. N.Y. Acad. Sci.* **55**, 548–573
25. Perey, B., Clermont, Y., and Leblond, C. P. (1961) The wave of the seminiferous epithelium in the rat. *Am. J. Anat.* **108**, 47–77
26. Dym, M., and Clermont, Y. (1970) Role of spermatogonia in the repair of the seminiferous epithelium following x-irradiation of the rat testis. *Am. J. Anat.* **128**, 265–282
27. Spengler, B., and Hubert, M. (2002) Scanning microprobe matrix-assisted laser desorption/ionization (SMALDI) mass spectrometry: instrumentation for sub-micrometer resolved LDI and MALDI surface analysis. *J. Am. Soc. Mass Spectrom.* **13**, 735–748
28. Monroe, E. B., Jurchen, J. C., Koszczuk, B. A., Losh, J. L., Rubakhin, S. S., and Sweedler, J. V. (2006) Massively parallel sample preparation for the MALDI MS analyses of tissues. *Anal. Chem.* **78**, 6826–6832
29. Zimmerman, T. A., Monroe, E. B., and Sweedler, J. V. (2008) Adapting the stretched sample method from tissue profiling to imaging. *Proteomics* **8**, 3809–3815
30. Zimmerman, T. A., Rubakhin, S. S., Romanova, E. V., Tucker, K. R., and Sweedler, J. V. (2009) MALDI mass spectrometric imaging using the stretched sample method to reveal neuropeptide distributions in aplysia nervous tissue. *Anal. Chem.* **81**, 9402–9409
31. Sugiura, Y., Setou, M., and Horigome, D. (2010) Methods of matrix application, in *Imaging Mass Spectrometry: Protocols for Mass Microscopy* (Setou, M., ed) pp. 71–86, Springer, New York
32. Lemaire, R., Tabet, J. C., Ducoroy, P., Hendra, J. B., Salzter, M., and Fournier, I. (2006) Solid ionic matrices for direct tissue analysis and MALDI imaging. *Anal. Chem.* **78**, 809–819
33. Fournier, I., Wisztorski, M., and Salzter, M. (2008) Tissue imaging using MALDI-MS: a new frontier of histopathology proteomics. *Expert. Rev. Proteomics* **5**, 413–424
34. Walch, A., Rauser, S., Deininger, S. O., and Höfler, H. (2008) MALDI imaging mass spectrometry for direct tissue analysis: a new frontier for molecular histology. *Histochem. Cell Biol.* **130**, 421–434
35. Kaleta, B. K., van der Wiel, I. M., Stauber, J., Güzel, C., Kros, J. M., Luider, T. M., and Heeren, R. M. (2009) Sample preparation issues for tissue imaging by imaging MS. *Proteomics* **9**, 2622–2633
36. Luxembourg, S. L., Mize, T. H., McDonnell, L. A., and Heeren, R. M. (2004) High-spatial resolution mass spectrometric imaging of peptide and protein distributions on a surface. *Anal. Chem.* **76**, 5339–5344
37. Schwartz, S. A., Reyzer, M. L., and Caprioli, R. M. (2003) Direct tissue analysis using matrix-assisted laser desorption/ionization mass spectrometry: practical aspects of sample preparation. *J. Mass Spectrom.* **38**, 699–708
38. Lemaire, R., Wisztorski, M., Desmons, A., Tabet, J. C., Day, R., Salzter, M., and Fournier, I. (2006) MALDI-MS direct tissue analysis of proteins: Improving signal sensitivity using organic treatments. *Anal. Chem.* **78**, 7145–7153
39. Seeley, E. H., Oppenheimer, S. R., Mi, D., Chaurand, P., and Caprioli, R. M. (2008) Enhancement of protein sensitivity for MALDI imaging mass spectrometry after chemical treatment of tissue sections. *J. Am. Soc. Mass Spectrom.* **19**, 1069–1077
40. Aerni, H. R., Cornett, D. S., and Caprioli, R. M. (2006) Automated acoustic matrix deposition for MALDI sample preparation. *Anal. Chem.* **78**, 827–834
41. Puolitaival, S. M., Burnum, K. E., Cornett, D. S., and Caprioli, R. M. (2008) Solvent-free matrix dry-coating for MALDI imaging of phospholipids. *J. Am. Soc. Mass Spectrom.* **19**, 882–886
42. Jégou, B., and Sharpe, R. M. (1993) Paracrine mechanisms in testicular control, in *Molecular Biology of the Male Reproduction System* (de Kretser, D. M., ed) pp. 271–310, Academic Press, New York
43. Jégou, B. (1993) The Sertoli-germ cell communication network in mammals. *Int. Rev. Cytol.* **147**, 25–96
44. Sharpe, R. M. (1994) Regulation of spermatogenesis, in *The Physiology of Reproduction* (Knobil, E., and Neill, J. D., eds) 2nd Ed., pp. 1363–1436, Raven Press, New York
45. Zhao, G. Q., and Garbers, D. L. (2002) Male germ cell specification and differentiation. *Dev. Cell* **2**, 537–547
46. Gnassi, L., Fabbri, A., and Spera, G. (1997) Gonadal peptides as mediators of development and functional control of the testis: an integrated system with hormones and local environment. *Endocr. Rev.* **18**, 541–609
47. Jégou, B., Pineau, C., and Dupaix, A. (1999) Paracrine control of testis function, in *Male Reproductive Function. Endocrine Update Series* (Wang, C., ed) pp. 41–64, Kluwer Academic, Berlin
48. Rolland, A. D., Jégou, B., and Pineau, C. (2008) Testicular development and spermatogenesis: harvesting the postgenomics bounty. *Adv. Exp. Med. Biol.* **636**, 16–41
49. Erickson-Viitanen, S., Ruggieri, S., Natalini, P., and Horecker, B. L. (1983) Thymosin beta 10, a new analog of thymosin beta 4 in mammalian tissues. *Arch. Biochem. Biophys.* **225**, 407–413
50. Lin, S. C., and Morrison-Bogorad, M. (1991) Cloning and characterization of a testis-specific thymosin beta 10 cDNA. Expression in post-meiotic male germ cells. *J. Biol. Chem.* **266**, 23347–23353
51. Monpezat, J. P., and Frindel, E. (1989) Further studies on the biological activities of the CFU-S inhibitory tetrapeptide AcSDKP. I. The precise point of the cell cycle sensitive to AcSDKP. Studies on the effect of AcSDKP on GM-CFC and on the possible involvement of T-lymphocytes in AcSDKP response. *Exp. Hematol.* **17**, 1077–1080
52. Stéphane, J., Melaine, N., Ezan, E., Hakovirta, H., Maddocks, S., Toppari, J., Garnier, D., Wdzieczak-Bakala, J., and Jégou, B. (2000) Source, catabolism and role of the tetrapeptide N-acetyl-Ser-Asp-Lys-Pro within the testis. *J. Cell Sci.* **113**, 113–121
53. Tang, P. Z., Tsai-Morris, C. H., and Dufau, M. L. (2001) Cloning and characterization of a hormonally regulated rat long chain acyl-CoA synthetase. *Proc. Natl. Acad. Sci. U.S.A.* **98**, 6581–6586
54. Hankin, J. A., Barkley, R. M., and Murphy, R. C. (2007) Sublimation as a method of matrix application for mass spectrometric imaging. *J. Am. Soc. Mass Spectrom.* **18**, 1646–1652
55. Russell, L. D., Ettlin, R. A., Sinha Hikim, A. P., and Clegg, E. D. (1990) *Histological and Histopathological Evaluation of the Testis*, Cache River Press, Clearwater, FL